Journal of Power Sources 200 (2012) 83–91

Contents lists available at SciVerse ScienceDirect

Journal of Power Sources

journal homepage: www.elsevier.com/locate/jpowsour

Influence of graphite surface modifications on the ratio of basal plane to "non-basal plane" surface area and on the anode performance in lithium ion batteries

T. Placke*, V. Siozios, R. Schmitz, S.F. Lux, P. Bieker, C. Colle, H.-W. Meyer, S. Passerini, M. Winter**

Institute of Physical Chemistry, MEET, University of Muenster, Corrensstr. 46, D-48149 Muenster, Germany

ARTICLE INFO

Article history:
Received 29 July 2011
Received in revised form 6 September 2011
Accepted 24 October 2011
Available online 28 October 2011

Keywords:
Lithium ion batteries
Graphite anode
Surface modification
Solid electrolyte interphase (SEI)
Nitrogen adsorption
Adsorptive potential distribution

ABSTRACT

For graphitic carbons as anode materials in lithium ion batteries, the morphology and chemistry of the graphite surface have a significant impact on the formation of the solid electrolyte interphase (SEI), the corresponding irreversible charge losses, and the overall electrochemical anode performance. In this work the effects of graphite surface modification, induced by an elevated temperature treatment, on the SEI formation are discussed in details. Morphology changes due to burn-off of carbon are investigated by Raman spectroscopy and nitrogen adsorption measurements, which are not only used to calculate the BET specific surface area but also for the estimation of the absolute and relative extents of the basal plane surface area and the "non-basal plane surface" area. In particular, the relation of the first cycle irreversible charge loss to the change of surface morphology, especially to the quantitative amounts of the different types of surfaces is highlighted.

1. Introduction

Graphitic carbons are the most commonly used anode materials for commercial lithium ion batteries, which is mainly due to a combination of sufficiently high specific capacity, very negative redox potential and outstanding dimensional stability [1]. Since lithium ion cells typically operate beyond the thermodynamic stability window of the organic electrolytes, electrolyte decomposition occurs. Fortunately, the decomposition products form a protective film at the carbon electrolyte interface which, in an ideal, practically not fully realized case, will act as an electronically insulating layer, thus stopping further electrolyte decomposition, while still permitting the transport of lithium ions. This lithium-ion conductive film behaves as a solid electrolyte interphase (SEI) [2]. The SEI formation, however, is associated with the irreversible consumption of materials (lithium and electrolyte), whereby the corresponding irreversible charge loss is called "irreversible capacity" (C_{irr}). This irreversible capacity due to the SEI formation mainly takes place in the first few charge/discharge cycles of cell operation, but does also affect the long-term cycling stability and calendar life [1,3–6].

As the lithium loss associated to C_{irr} reduces the specific energy of the cell, it is advantageous to reduce C_{irr} while still forming an effective and thin SEI. The formation of the SEI largely depends on the electrode surface accessible to the electrolyte. Basically, this surface is determined by the electrode morphology (type of binder, porosity, etc.) and the type of graphitic/carbonaceous compound used. Carbons are characterized by different surface properties, e.g. surface area, particle size distribution and particle shape [6–9].

Graphitic carbons principally possess two different kinds of surfaces, basal plane and prismatic (edge) surfaces. Whereas ideal (defect and contaminant free) basal plane surfaces are homogeneous ("smooth") and consist only of carbon atoms, the prismatic surfaces are heterogeneous ("rough") and, beside carbon, contain various surface groups, mostly oxygen containing. It is well known that the basal plane and prismatic surfaces of graphite exhibit different physical and chemical behavior in many regards [10,11], which also has a significant impact on the electrochemical reactivity in lithium ion batteries [7,12]. This is due to the fact that the transport of lithium ions during charge/discharge operation takes place via the prismatic surfaces rather than the basal plane surfaces [13]. Therefore, the ratio of the basal plane surface area to the "non-basal plane surface" area is an important factor in determining the dependence of irreversible charge losses to the specific surface area [11,14].

* Corresponding author. Tel.: +49 251 83 36701; fax: +49 251 83 36032.
** Corresponding author. Tel.: +49 251 83 36031; fax: +49 251 83 36032.
E-mail addresses: tobias.placke@uni-muenster.de (T. Placke), martin.winter@uni-muenster.de (M. Winter).

0378-7753/$ – see front matter © 2011 Elsevier B.V. All rights reserved.
doi:10.1016/j.jpowsour.2011.10.085

Apart from graphite surface modifications like carbon coatings or formation of composites with metal oxides [15–17], one route to decrease the irreversible capacity and improve the performance of graphite anodes is to chemically treat the surface of graphite either by employing oxidative solutions like H_2O_2, $Ce(SO_4)_2$, HNO_3 or $(NH_4)_2S_2O_8$ [18,19] or by treatment with CO_2, O_2 or other gases at elevated temperatures [7,12,20–22]. Whereas the ideal basal planes are rather inert towards gaseous treatments, the surface chemistry and morphology of the "non-basal surfaces" as well as the anode performance may be changed significantly [7].

Here, we present the effects of graphite surface treatments with oxygen at various temperatures on the graphite surface properties and on the consequences for the SEI formation. Morphology changes of the graphitic carbons are investigated using Raman spectroscopy and nitrogen adsorption measurements. From evaluation of the nitrogen adsorption data it is possible to individually estimate the absolute and relative extents of the prismatic and basal plane surfaces by employing a deconvolution technique. This method, developed by Ross and Olivier, is based on a model for describing adsorption on energetically heterogeneous surfaces of the same compound [14,23,24]. The heterogeneous graphite surface can be described by a distribution of adsorptive potentials that are represented by a continuous distribution function. The evaluation of this function by using the non-local density functional theory (DFT) is described elsewhere [14,25]. Thus, it is possible to point out the correlation of the irreversible capacity to the nature of the graphitic surface and to define the influence of each temperature treatment directly to the ratio of the surfaces and to the SEI formation. The correlation of these parameters leads to an optimized temperature treatment in order to decrease the irreversible charge losses in the first cycles.

2. Experimental

2.1. Synthesis of O_2-modified graphites

Synthetic graphite TIMREX® SLP30 (TIMCAL®, d_{50} = 16.0 μm/d_{90} = 32.0 μm) was heated under oxygen flow in a quartz glass tube placed in a tube furnace, by increasing the temperature from room temperature up to the desired temperature with a heating rate of 100 °C h^{-1}. Afterwards, the samples were kept under oxygen flow at the desired temperature for three hours. After treatment, the furnace and the quartz glass tube therein were cooled down to room temperature under oxygen flow again.

2.2. Scanning electron microscopy (SEM)

SEM investigations of the pristine and modified graphite powders have been performed with an Auriga® scanning electron microscope by Carl Zeiss NTS GmbH, operating at a nominal acceleration voltage of 5 keV that has proved optimum conditions for the investigation of the graphite specimens.

2.3. Nitrogen adsorption measurements

Nitrogen adsorption measurements were performed at liquid nitrogen temperature (77.3 K) using an ASAP 2020 (Accelerated Surface Area and Porosimetry Analyzer) apparatus by Micromeritics Instrument Corporation. Before measurement the samples were degassed at 443 K until a static vacuum of less than 0.01 Torr was reached. To calculate the adsorptive potential distributions from the adsorption isotherms the standard instrument software (version 3.03) was employed and the DFT Plus® (MNLDFT) software was used.

2.4. Raman spectroscopy

A Bruker SENTERRA dispersive microscope was used to analyze the graphite surface properties. The laser source was a semiconductor-laser operating at a wavelength of 532 nm. The laser power was adjusted by a filter to 10 mW. A grating of 400 lines mm^{-1} was used. The aperture was a slit with a dimension of 50 × 1000 μm. The lasers as well as the spectrometer were calibrated with a neon lamp. The detector was a CCD detector with 1024 × 256 pixels, which was thermoelectrically cooled to −65 °C. For the microscope, a 20× objective was used. To collect the spectra 10 integrations were carried out with an integration time of one second.

2.5. Thermogravimetry analysis (TGA)

The thermogravimetric measurements were carried out on a TGA Q5000 IR system by TA instruments. The graphite powders were heated up to 1000 °C in platinum pans with a heating rate of 25 °C min^{-1}. The weight change curves of the various graphite samples were collected under nitrogen atmosphere.

2.6. Electrode preparation

Electrode tapes were prepared using a composition of 95 wt.% of active material (either pristine or heat-treated graphite) and 5 wt.% poly(vinylidene)fluoride binder (PVdF, Kynar® 761). Prior to the dispersion of the active material, the binder polymer was dissolved in anhydrous, high-purity *N*-methyl pyrrolidone (NMP) to obtain a 4.0 wt.% solution. The pristine or modified SLP30 graphite was added to the binder solution and dispersed using a T 25 Ultra Turrax® (1 h, 5000 rpm) to eliminate possible agglomerates and homogenize the paste. Afterwards, the electrode paste was cast on a high purity copper foil (Carl Schlenk AG®) using the doctor-blade technique. The gap of the doctor blade was chosen to be 100 μm leading to an average mass loading of 5 mg cm^{-2}. The tapes were immediately transferred into an atmospheric oven and dried for 12 h at 80 °C. A further drying step was done in a BÜCHI® oven under an oil-pump vacuum at 120 °C for 24 h. Thereafter, the tapes were stored in an Argon filled glove box (UniLab, MBraun) with water and oxygen contents below 1 ppm.

2.7. Electrochemical measurements

The electrochemical investigations were carried out in Swagelok® type T-cells with a three electrode setup. The measurements were performed in a half-cell setup using high-purity metallic lithium foil (Chemetall®) both as reference and counter electrodes. As separator a stack of polypropylene fleeces (Freudenberg® FS2226) drenched with 120 μL of electrolyte was used. The electrolyte used in all investigations was a 3:7 wt.% mixture of ethylene carbonate (EC): diethylene carbonate (DEC) with 1 M lithium hexafluorophosphate ($LiPF_6$) as conductive salt. The water content of the electrolytic solution determined by Karl Fischer titration was less than 10 ppm. Charge–discharge cycling was carried out using a multichannel Maccor 4300 battery test system. To investigate the irreversible capacities in the first cycles, the charge and discharge steps were performed using a constant current which corresponds to a C/20 (0.09 mA) charge/discharge rate. The charging process (lithium intercalation) was carried out down to a cut-off potential of 20 mV vs. Li/Li^+ while for the discharging process (de-lithiation) a cut-off potential of 1500 mV vs. Li/Li^+ was chosen. To ensure the reproducibility of the electrochemical performance, each graphite sample was cycled independently for at least four times under these conditions. The calculation of the errors in Table 5 and Fig. 8 is based on the standard deviation of the average

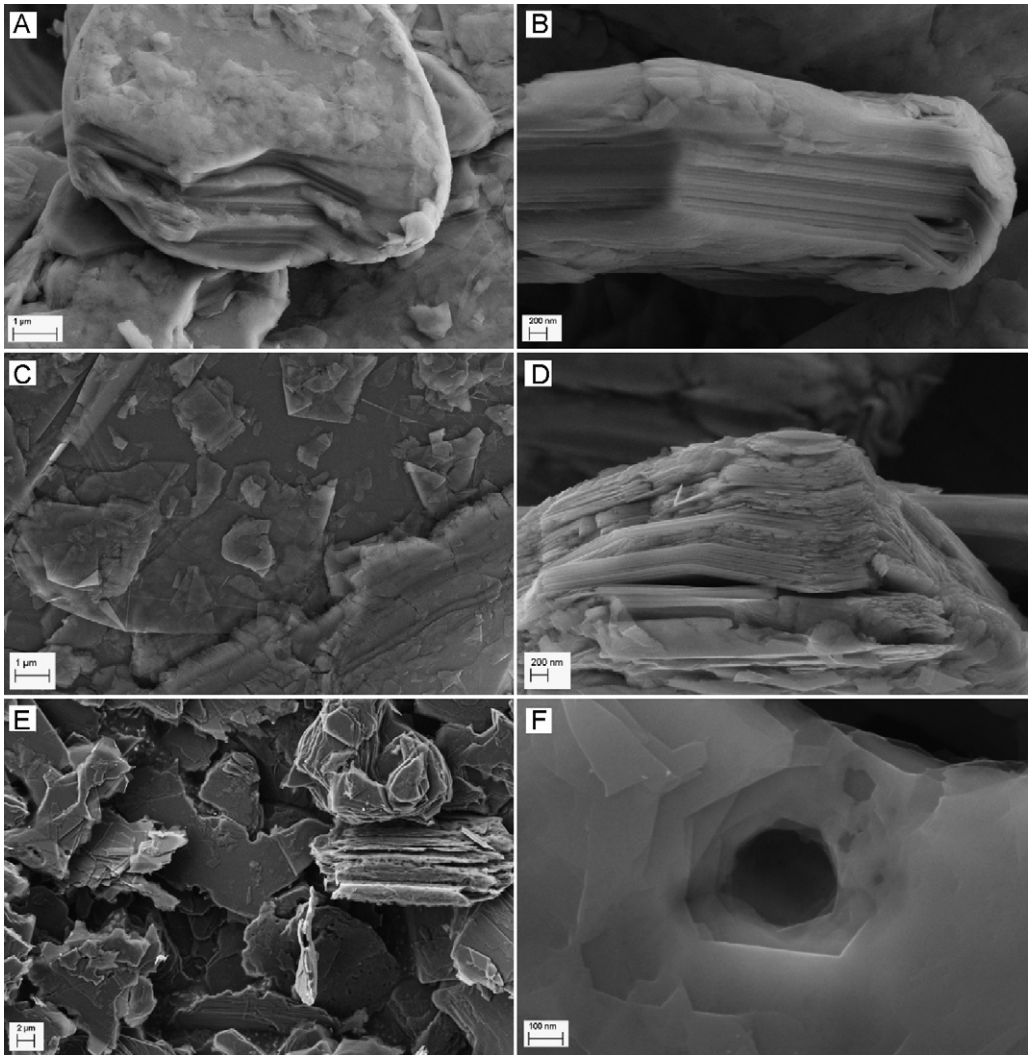

Fig. 1. SEM images of TIMREX® SLP30 graphites: (A) and (B) pristine SLP30 graphite; (C) and (D) after oxygen heat-treatment at 480 °C; (E) and (F) after oxygen heat-treatment at 580 °C.

values for efficiency and irreversible capacity of the independently cycled cells.

3. Results and discussion

3.1. Mild and strong oxidation of graphite with oxygen

For the surface heat-treatment of SLP30 graphite four different oxidation temperatures between 480 °C and 580 °C were chosen to investigate the influence of the oxidation on the graphite surface properties and on their electrochemical properties as anode material. Table 1 shows the weight loss (burn-off) of SLP30 graphite during the heat-treatment (see experimental) at different oxidation temperatures. At temperatures below 500 °C oxygen is slowly combusting carbon, leading to a burn-off of about 3–6 wt.%. At temperatures above 500 °C oxygen acts as a strong oxidation agent, leading to high combustions. At 540 °C the burn-off is already above 20 wt.% and at 580 °C the weight loss is more than 50 wt.%.

Table 1
Weight loss of graphite after oxygen heat-treatment at different temperatures.

O_2 heat-treated graphites	Burn-off (%)
SLP30-480 °C	3.4
SLP30-500 °C	6.7
SLP30-540 °C	21.0
SLP30-580 °C	54.5

3.2. Morphology and surface characteristics of pristine and modified graphites

Fig. 1 compares representative SEM images of pristine SLP30 graphite (panel A and B), with those of oxygen heat-treated samples at a mild oxidation temperature of 480 °C (panel C and D) and at an elevated temperature of 580 °C (panel E and F). SLP30 graphite displays its typically potato-shape morphology with an average particle size of about 16.0 μm. The pristine SLP30 graphite provides a surface morphology with a large degree of surface heterogeneity (Fig. 1, panel A). It is observable that especially the basal plane surfaces of the graphite particles provide no homogeneous surfaces. Instead, they show a large number of "defects" or disordered-like arrangements leading to a certain degree of "surface roughness". This kind of surface roughness is also observable at the edge (prismatic) surfaces of the graphite particles where at the bottom and the top layers round shapes instead of graphite-typical planar structures are observed (Fig. 1, panel B). The SEM images for the oxygen heat-treated graphite under mild conditions (480 °C) clearly indicate changes in the surface morphology due to the

Table 2
BET surface areas, DFT surface areas, prismatic, basal plane and "defect" surface areas, "non-basal plane surface" areas, ratio of prismatic surface area to basal plane surface area to "defect surface" area and ratio of basal plane surface area to "non-basal plane surface" area of pristine and O_2 heat-treated graphites, derived from nitrogen adsorption data.

	SLP30 pristine	SLP30-480 °C	SLP30-500 °C	SLP30-540 °C	SLP30-580 °C
BET surface area ($m^2\ g^{-1}$)	6.89	6.73	5.82	4.40	3.68
DFT surface area ($m^2\ g^{-1}$)	7.12	6.97	5.88	4.60	4.07
Prismatic surface area ($m^2\ g^{-1}$)	2.79	1.57	1.46	1.07	1.43
Basal plane surface area ($m^2\ g^{-1}$)	3.49	4.78	4.08	3.53	2.64
"Defect surface" area ($m^2\ g^{-1}$)	0.84	0.62	0.34	0	0
"Non-basal plane surface" area ($m^2\ g^{-1}$)	3.63	2.19	1.80	1.07	1.43
Ratio of prismatic surface area (%):basal plane surface area (%):"defect surface" area (%)	39.2:49.0:11.8	22.5:68.6:8.9	24.8:69.4:5.8	23.2:76.8:0	35.1:64.9:0
Ratio of basal plane surface area (%):"non-basal plane surface" area (%)	49.0:51.0	68.6:31.4	69.4:30.6	76.8:23.2	64.9:35.1

burn-off. Regarding the basal plane surfaces, there are several "defect arrangements" which are separated by sharp edges, indicating that mainly external prismatic surfaces are attacked by the oxidation process (Fig. 1, panel C). This can also be observed by having a direct view at the prismatic surfaces of the graphite particles (Fig. 1, panel D) which clearly display changes in the sub-μm scale roughness compared to the edge surfaces of pristine SLP30 graphite. The SEM pictures for the strongly oxidized graphite (580 °C) obviously exhibit more extensive changes in the surface morphology. The basal plane surfaces provide decreased surface roughness and seem to be "cleaned" from the non-ordered "defect arrangements" by the combustion process (Fig. 1, panel E). However, by this strong oxidation process the prismatic surfaces are severely attacked leading to "layer-like" prismatic surface morphologies, similar to exfoliated graphite. In addition, even the basal plane surfaces are deeply attacked and provide several pores with diameters up to 300 nm (Fig. 1, panel E and F).

The representative adsorptive potential distributions of pristine and oxygen heat-treated SLP30 graphites, calculated from the nitrogen adsorption data, are displayed in Fig. 2. Table 2 compares the surface areas for all graphite samples, calculated by two different methods, the BET and DFT methods. The differences between the BET and DFT surface areas for each sample are a result of the different kinds of assumptions made in their theories. The calculation of the BET surface area is based on the assumption that the surface of the solid adsorbent is absolutely homogeneous. However, graphitic carbons have a heterogeneous surface, providing basal plane surfaces, prismatic surfaces and "defect surfaces". This means that the surface area calculated via the BET theory, which is not accounting any surface heterogeneities, is not providing an absolute representative value of the surface area but only an approximate estimate [14]. Contrasting this method, the DFT surface area is calculated by a modified non-local density functional theory (MNLDFT software, by Ross and Olivier), which regards and estimates surface heterogeneities of solids. The premises of this model are that the surface of a real solid is composed of small patches that (i) adsorb nitrogen with different affinities (adsorptive potentials) and (ii) adsorb independently from each other. In addition, it is assumed that the distribution of adsorptive potentials among these small patches can be represented by a distribution function [14,23,24]. Pristine SLP30 graphite provides a quite broad adsorptive potential distribution in the range of about 40–90 K (unit of the adsorptive potential is Kelvin) which indicates a considerable surface heterogeneity (Fig. 2). From literature [14,26], it is known that the adsorptive potential distribution centered between 50 K and 60 K represents the basal plane surfaces. In the case of physical adsorption, the magnitude of the adsorptive potential depends largely on the local density of the adsorbent constituent atoms. The basal plane surfaces providing a higher areal carbon density will adsorb nitrogen more strongly than the less dense prismatic surfaces (Fig. 3, panel A and B). Therefore, in the adsorptive potential distribution the prismatic surfaces are represented by the lower surface energies. In contrast, lattice defects in the graphene layers of the basal plane surfaces, such as surface groups or surface steps as well as dislocations are resulting in an increased "surface roughness" which also enhances the adsorbent–adsorptive interactions and leads to higher adsorptive potentials than for the basal plane surfaces (Fig. 3, panel C). Polar surface groups, such as carboxy or carbonyl groups, may also enhance these interactions. In conclusion, for the nitrogen adsorption on graphitic carbons the following order determines the distribution of adsorptive potentials: prismatic surfaces < basal plane surfaces < surface roughness.

Table 3
Raman intensity ratios of D-band versus G-band of pristine and oxygen heat-treated SLP30 graphite at different temperatures.

Graphite	I_D/I_G
SLP30 pristine	0.47
SLP30-480 °C	0.15
SLP30-500 °C	0.15
SLP30-540 °C	0.11
SLP30-580 °C	0.11

For the BET and DFT surface areas of the graphite samples it is obvious that both are decreasing by increasing the oxidation temperature (Table 2). Whereas the pristine SLP30 graphite exhibits a specific BET surface area of about 6.9 $m^2\ g^{-1}$, the modified graphite at 580 °C provides a decreased value of about 3.7 $m^2\ g^{-1}$. By integration under the increments (Fig. 2), it is possible to determine the absolute and relative extents of each kind of surface for the different graphite samples. Table 2 displays the incremental surface areas for the basal plane, prismatic and "defect" surfaces and the relative percental ratio of these surfaces. Additionally, the ratio of the basal plane surface area to the "non basal plane surface" area, which accumulates both the prismatic and "defect surface" area, is illustrated. From the calculated data, changes in these ratios between the different graphite samples can clearly be observed. By increasing the oxidation temperature, the amount of "defect surface" area is decreased from about 12% for the pristine graphite to about 0% for the sample heat-treated at 540 °C. This can also be observed in the adsorptive potential distributions (Fig. 2) where the surface heterogeneity, especially at high adsorptive potentials, is reduced. Another trend is observable for the pristine and the heat-treated graphites at 480 °C, 500 °C and 540 °C. In this oxidation range the amount of prismatic surface area is decreased from 39% to about 23% whereas the amount of basal plane surface area increases from 49% to about 77%. Regarding the highest oxidation temperature of 580 °C there is a change in this trend because the amount of prismatic surface area clearly increases to about 35% whereas the amount of basal plane surface area decreases to 65%. A possible explanation for the observed change of the incremental

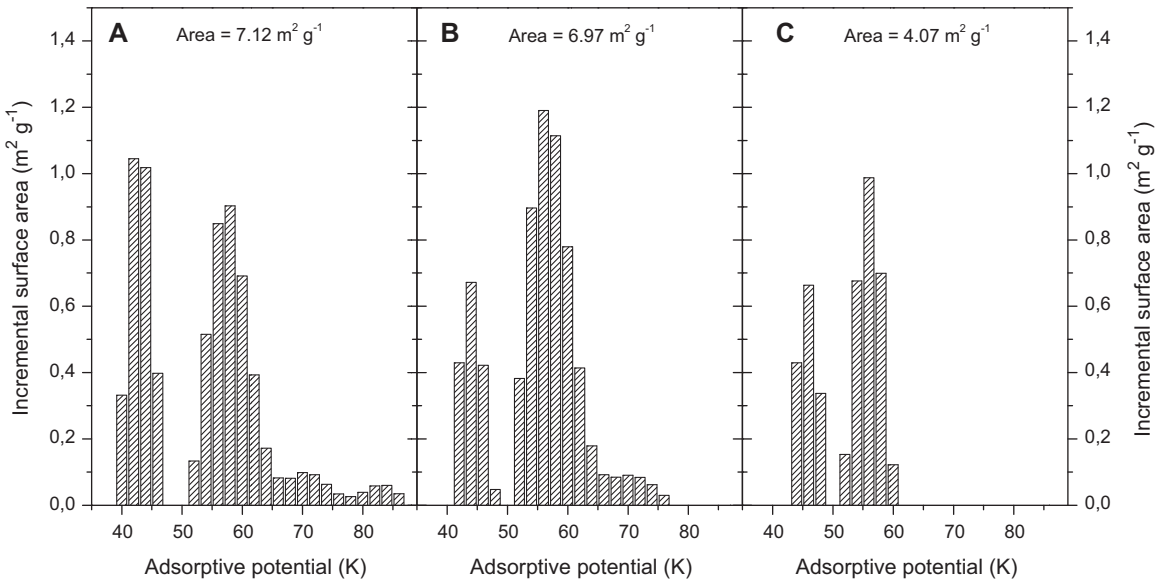

Fig. 2. Incremental surface area vs. adsorptive potential plots of pristine SLP30 graphite (A), oxygen heat-treated SLP30 graphite at 480 °C (B) and oxygen heat-treated SLP30 graphite at 580 °C (C).

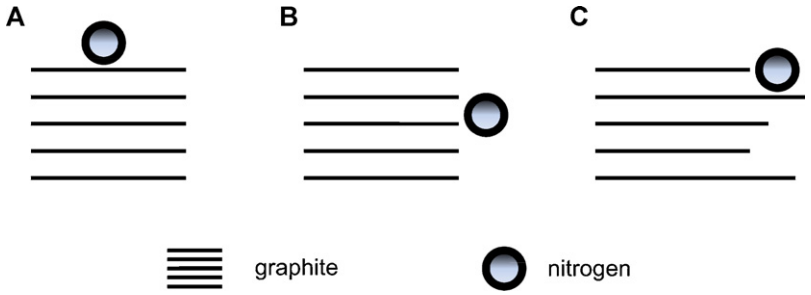

Fig. 3. Scheme for the nitrogen adsorption on different kinds of graphitic carbon surfaces: nitrogen adsorption on basal plane surfaces (A), prismatic surfaces (B) and "defect surfaces" or dislocations leading to surface roughness (C).

surface areas at high temperatures can be seen in Fig. 4, showing a scheme for the combustion process under mild and strong conditions. Under mild conditions the oxidation mainly takes place at the prismatic and "defect" surfaces of the graphitic surface, correlating to the results from SEM images and DFT calculations. At strong oxidation conditions (580 °C) it is indicated that not only the prismatic surfaces, but also the basal plane surfaces are attacked by the oxygen. This harsh treatment leads to the formation of large

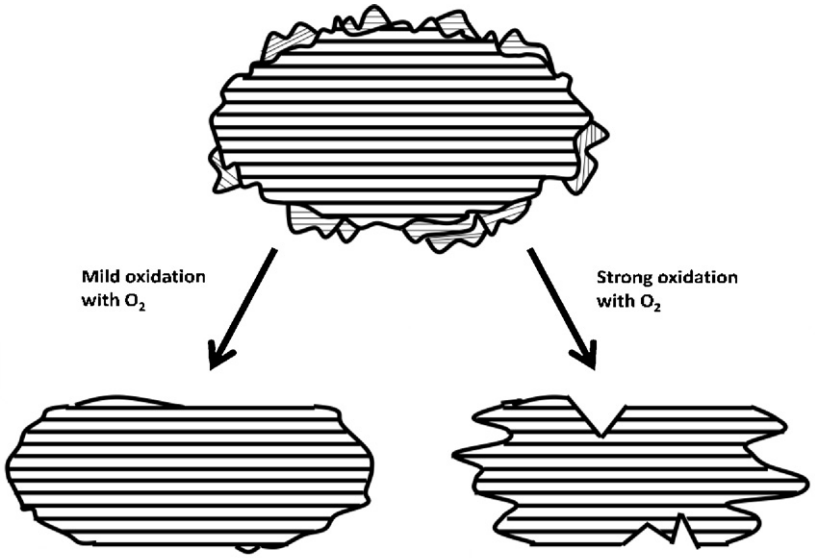

Fig. 4. Scheme for the combustion process of graphite by oxygen heat-treatment under mild (left) and strong (right) oxidation conditions.

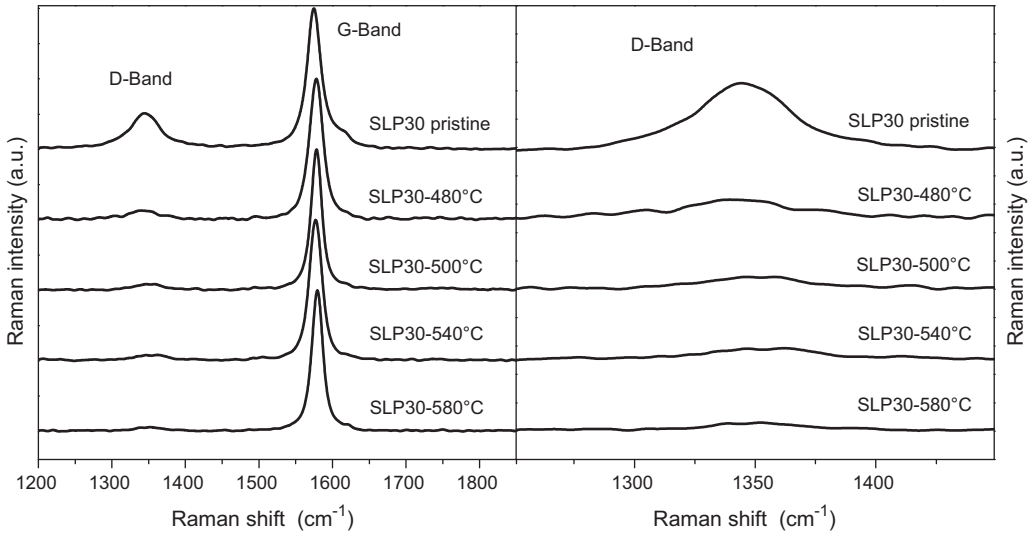

Fig. 5. Results of the Raman spectroscopic studies performed on pristine TIMREX® SLP30 graphite and on oxygen heat-treated SLP30 graphite at various temperatures.

pores in the basal plane surfaces (Fig. 4, right) of the graphite particles that can also be observed in the SEM pictures (Fig. 1, panel F). These pores, having sizes of up to 300 nm, and the strongly attacked prismatic surfaces (Fig. 1, panel E) seem to result in an increased amount for the prismatic surface area, as derived from DFT calculations.

Raman spectroscopy has proven to be a powerful technique in studying the texture of pure graphite materials [27]. A typical Raman spectrum of graphite consists of two E_{2g} active modes corresponding to the in-plane vibrations of the carbon atoms, a strong G-band at about 1582 cm^{-1} (E_{2g2}) and a weak band at 42 cm^{-1}, which is difficult to observe [28]. Microcrystalline graphite materials provide additional bands at about 1360 cm^{-1} (D-band) and 1623 cm^{-1} (D′-band) which correspond to the crystal boundary regions. The D-band is associated with a symmetry break at the edges of graphene sheets and thus increases with an increasing amount of disordered arrangements on the graphite particle surface [27,28]. Fig. 5 displays the results of the Raman measurements of pristine and modified SLP30 graphite. The Raman spectra clearly indicate changes between the pristine and modified SLP30 graphites. The D-band of all oxygen heat-treated graphites is considerably decreased compared to pristine graphite. This result can also be observed by regarding the Raman intensity ratios of D-band versus G-band of pristine and modified graphites in Table 3. For pristine SLP30 graphite the I_D/I_G ratio provides a value of 0.47 whereas this value is decreased to about 0.15 for the modified graphites. The results from Raman measurements correlate with the results from the SEM investigations and DFT calculations. The oxygen treatment leads to a decreased D-band which is related to a decreased amount of disordered or amorphous carbon on the graphite surface. This result is also observable in the SEM images and in the adsorptive potential distributions, providing a decreased amount of surface defects by the oxygen treatment.

Thermogravimetric analysis was used to investigate the thermal stability as well as the amount of functional groups of pristine and modified graphites. Fig. 6 displays the results of thermogravimetric analysis for pristine SLP30 graphite and two representative modified graphites, one at low combustion temperature of 480 °C and one at elevated temperature of 580 °C. Table 4 shows the corresponding weight losses of each graphite sample, calculated in the temperature range from room temperature up to 1000 °C. For all samples the weight loss in this temperature range is less than 1%. However, there are differences between the untreated and modified samples. Whereas the pristine SLP30 graphite provides a value of 0.25 wt.% weight loss, the modified samples exhibit decreased values of about 0.08 wt.% (Fig. 6, Table 4). These decreased values suggest a lower concentration of functional groups on the graphite surface. Relating to the previous results it seems that a decreased amount of surface "defects" and the possible removal of surface impurities by oxygen treatment lead to a thermally more stable graphite surface structure [29].

Table 4
Weight loss of pristine and oxygen heat-treated SLP30 graphite at different temperatures, derived from thermogravimetric analysis under nitrogen atmosphere and a heating rate of 25 °C min^{-1}. Weight losses correspond to the range from room temperature up to 1000 °C.

Graphite	Weight loss (%)
SLP30 pristine	0.250
SLP30-480 °C	0.083
SLP30-500 °C	0.081
SLP30-540 °C	0.079
SLP30-580 °C	0.059

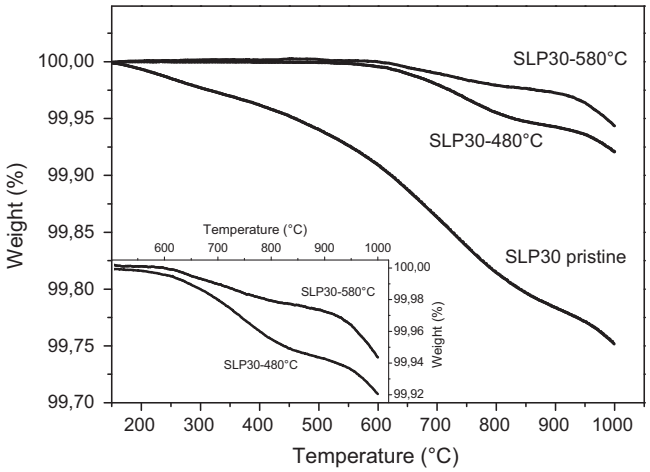

Fig. 6. Thermogravimetric analysis of pristine TIMREX® SLP30 graphite and oxygen heat-treated SLP30 graphite (at 480 °C and 580 °C) under nitrogen atmosphere and a heating rate of 25 °C min^{-1}.

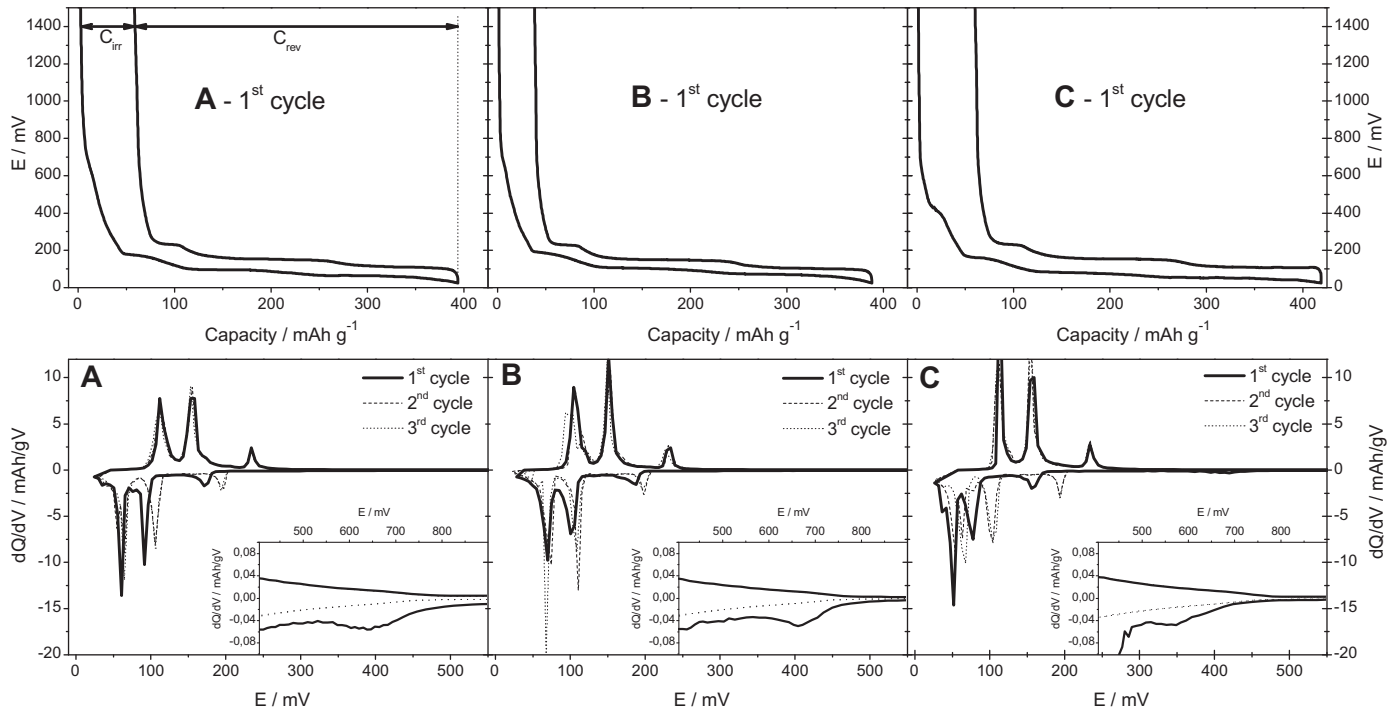

Fig. 7. Representative curves for the electrochemical investigations of pristine and two oxygen heat-treated graphites with charge and discharge corresponding to 0.05C (A): pristine SLP30 graphite, (B): SLP30-540 °C, (C): SLP30-580 °C. Top part: Charge–discharge curves of corresponding graphites in 1st first cycle. Bottom part: Differential capacity plots of corresponding graphites in the first three cycles; small insets display the range where the main SEI formation/electrolyte reduction in the first cycles takes place.

3.3. Electrochemical performance of pristine and modified graphites

Fig. 7 displays the results for the electrochemical measurements of pristine SLP30 graphite (panel A) and two representative modified graphites at 540 °C (panel B) and 580 °C (panel C). The upper part shows the corresponding charge–discharge curves in the first cycle where differences in the charge and discharge characteristics can be observed. Especially the charge curves in the range between 500 mV and 200 mV vs. Li/Li^+, before bulk lithium intercalation and stage formation take place [1], exhibit differences. For the modification at 580 °C an additional peak at about 500 mV vs. Li/Li^+ can be observed. The four graphite-typical lithium intercalation steps are located in the range between 200 mV and 20 mV vs. Li/Li^+. The lower part of Fig. 7 displays the differential capacity plots of the above mentioned graphite samples in the first three cycles. From these plots it can be clearly observed that the main part of the SEI formation takes places in the first cycle, as in the second and third cycle the charge–discharge curves only provide slight differences in their characteristics. The small insets show the differences in the charge–discharge curves for the first three cycles in the range between 900 mV and 400 mV vs. Li/Li^+. It is known that the main part of C_{irr} due to SEI formation via electrolyte decomposition takes place in the range between 800 mV and 200 mV vs. Li/Li^+ [30]. The differences in the first cycle charge loss between the three representative samples can be clearly observed, with the oxygen modification at 540 °C providing the lowest C_{irr} (Fig. 7, panel B).

Table 5 displays the charge and discharge capacities and the corresponding discharge/charge efficiencies for the first three cycles as well as the irreversible capacities in cycle 1–3 for all investigated graphite samples. Pristine SLP30 graphite provides a first cycle efficiency of 85.2%, whereas the modification at 480 °C exhibits an increased efficiency of 88.5%. The first cycle efficiency shows the highest value for the modification at 540 °C with 90.1%. This tendency of decreased irreversible charge loss by oxygen heat-treatment of graphite can be even more clearly observed by regarding the values of irreversible capacity in the first three cycles. The pristine SLP30 graphite exhibits a value of 19.4% (74.5 mAh g^{-1}) which is decreased to 12.3% (46.8 mAh g^{-1}) in the modification temperature range from 480 °C to 540 °C. For the highest investigated modification temperature of 580 °C the first cycle efficiency is decreased to 85.6% and the irreversible charge loss in cycle 1–3 increased to 17.9% (73.1 mAh g^{-1}). The discharge capacities are providing values of 340 mAh g^{-1} for pristine SLP30 graphite and slightly increased discharge capacities of 350–360 mAh g^{-1} for the modified graphite anodes.

To correlate the electrochemical results with the physical properties of the investigated graphite samples, such as the specific surface area, it has to be mentioned that from literature it is known that there is an approximately linear relationship between the specific surface area (determined by BET method) and irreversible charge consumption in the first cycle [11,31]. However, it is also known that the reactions at the prismatic and "defect" surfaces, such as solvated lithium intercalation, exfoliation of graphene sheets or self-discharge reactions contribute much more to the total charge loss than reactions on the basal plane surfaces [10,11]. Thus, the ratio of the basal plane surface area to the "non-basal plane surface" area is an important factor in determining the dependence of irreversible capacity to the specific surface area [14]. Fig. 8 displays the irreversible charge loss in the 1st cycle of the investigated graphites as a function of the BET and DFT surface area (Fig. 8, panel A). For the pristine graphite and the three modifications in the temperature range of 480–540 °C an approximately linear relationship of increasing C_{irr} with increasing DFT and also BET surface area can be observed. However, this is not true for the graphite modification at 580 °C. Even though this sample exhibits the lowest DFT specific

Table 5
Specific charge and discharge capacities, irreversible capacities, discharge/charge efficiencies for the first three cycles and irreversible capacities for cycles 1–3 of pristine and oxygen heat-treated graphite anodes, obtained from constant current cycling data.

	Cycle number	Charge capacity ($mAh\,g^{-1}$)	Discharge capacity ($mAh\,g^{-1}$)	Irreversible capacity (%)	Efficiency (%)	Irreversible capacity in cycle 1–3 (%)
SLP30 pristine	1	393.7	335.4	14.8 ± 0.4	85.2 ± 0.4	
	2	351.0	341.2	2.8 ± 0.3	97.2 ± 0.3	19.4 ± 1.0
	3	347.7	341.3	1.8 ± 0.3	98.2 ± 0.3	
SLP30-480 °C	1	392.4	347.1	11.5 ± 0.4	88.5 ± 0.4	
	2	365.3	358.1	2.0 ± 0.3	98.0 ± 0.3	14.7 ± 1.0
	3	364.9	360.4	1.2 ± 0.3	98.8 ± 0.3	
SLP30-500 °C	1	379.6	338.4	10.9 ± 0.3	89.1 ± 0.3	
	2	359.3	354.1	1.4 ± 0.3	98.6 ± 0.3	13.2 ± 0.9
	3	361.6	358.3	0.9 ± 0.3	99.1 ± 0.3	
SLP30-540 °C	1	388.2	349.9	9.9 ± 0.3	90.1 ± 0.3	
	2	359.3	353.9	1.5 ± 0.3	98.5 ± 0.3	12.3 ± 0.9
	3	360.0	356.9	0.9 ± 0.3	99.1 ± 0.3	
SLP30-580 °C	1	419.0	358.8	14.4 ± 0.5	85.6 ± 0.5	
	2	372.3	364.1	2.2 ± 0.3	97.8 ± 0.3	17.9 ± 1.1
	3	367.4	362.7	1.3 ± 0.3	98.7 ± 0.3	

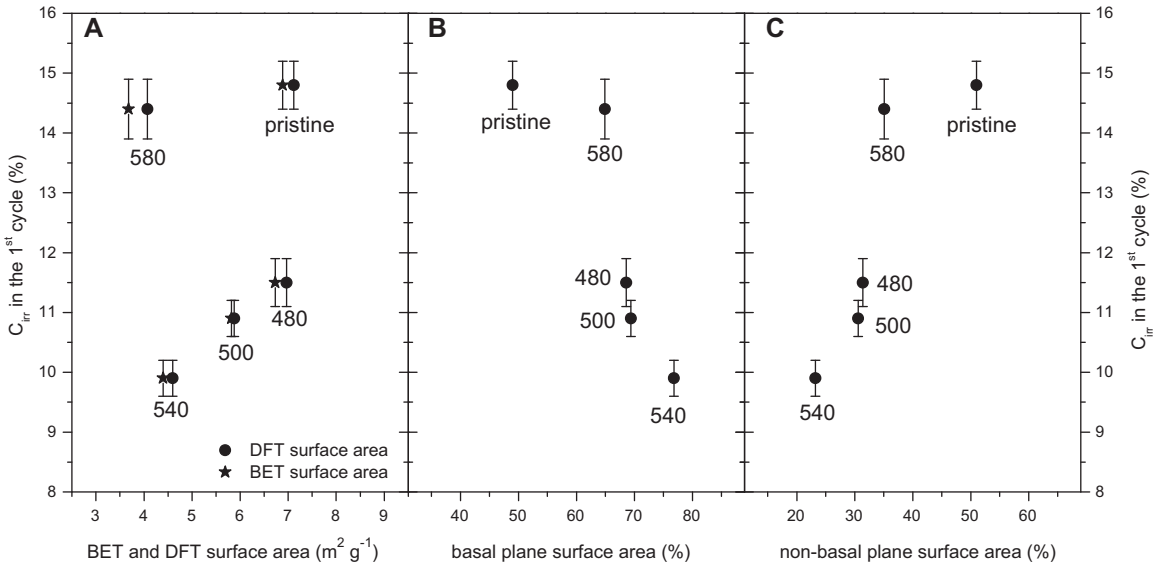

Fig. 8. Irreversible charge loss in the 1st cycle of pristine and oxygen heat-treated SLP30 graphites as a function of the BET and DFT surface area (A), of the basal plane surface area (B, percental values) and non-basal plane surface area (C, percental values).

surface area of $4.07\,m^2\,g^{-1}$, it provides an increased irreversible charge loss which is almost in the range of the pristine sample. Having a closer look at the dependence of irreversible capacity on the percental values of the basal plane surface area respective the "non-basal plane surface" area, approximately linear relationships can be observed (Fig. 8, panel B and C). C_{irr} increases nearly linearly with an increasing ratio of "non-basal plane surface" area respective decreases with an increasing ratio of basal plane surface area. In conclusion, it has to be mentioned that the specific surface areas of graphites (by BET or DFT method) seems not always to provide a linear relationship to the irreversible charge losses. The ratio of basal plane to "non-basal plane surface" area has to be regarded as the prismatic and "defect" surface areas contribute much more to C_{irr}. In addition, it has to be taken into account that other effects, such as the electrode structure (different electrode densities, different coverage of graphite particles with binder, different contact zones with binder and electrolyte) can influence this relationship also. However, these influences were tried to keep as small as possible by using the same preparation procedure for all investigated graphite samples.

4. Conclusion

A systematic method for graphite surface modifications by oxygen treatment at elevated temperatures has been presented. By refinement of the correlation between the irreversible capacity to the graphite surface properties, especially to the nature of the graphitic surface, it is possible to obtain an optimized temperature treatment in order to decrease the irreversible charge loss in the first cycles.

DFT calculations, derived from nitrogen adsorption data, allow the determination of surface heterogeneities of graphitic carbons by adsorptive potential distribution. Thereby, it is possible to calculate the absolute and relative extents of basal plane surfaces and "non-basal plane surfaces" (accumulating the prismatic and "defect surfaces") for the investigated graphite powders. Changes in the ratio of basal plane to "non-basal plane" surface area by surface modifications at elevated temperatures can easily be observed and correlated with the electrochemical performance. The changes observed in the adsorptive potential distributions are correlating with the results that were obtained by SEM, Raman spectroscopy

and thermogravimetric analysis regarding the surface morphology and surface texture of the investigated graphite powders. From the presented results it has to be pointed out clearly that a linear correlation between the specific surface area (calculated by BET or DFT method) and irreversible charge loss cannot be expected in all cases. However, a strong indication has been found that an approximately linear relationship between the irreversible capacity to the ratio of the "non-basal plane surface" area respective to the ratio of the basal plane surface area exists. C_{irr} increases approximately linear with the increasing ratio of the "non-basal plane surface" area and correspondingly decreases with an increasing ratio of the basal plane surface area.

By choosing an optimized temperature treatment for the investigated SLP30 graphite it was possible to increase the first cycle efficiency from about 85 to 90% and to correlate the electrochemical performance with the ratio of surfaces present in the graphite. Further investigations with different reactive gases and treatment parameters are in progress.

Acknowledgements

The authors wish to thank the German Ministry of Education and Research (BMBF) for funding of this work in the project "LiVe" (03X4601A) within the "LIB2015" research alliance.

References

[1] M. Winter, J.O. Besenhard, M.E. Spahr, P. Novak, Advanced Materials 10 (1998) 725–763.
[2] E. Peled, Journal of the Electrochemical Society 126 (1979) 2047–2051.
[3] J. Vetter, P. Novak, M.R. Wagner, C. Veit, K.C. Moller, J.O. Besenhard, M. Winter, M. Wohlfahrt-Mehrens, C. Vogler, A. Hammouche, Journal of Power Sources 147 (2005) 269–281.
[4] J.O. Besenhard, M. Winter, J. Yang, W. Biberacher, Journal of Power Sources 54 (1995) 228–231.
[5] S.S. Zhang, M.S. Ding, K. Xu, J. Allen, T.R. Jow, Electrochemical and Solid State Letters 4 (2001) A206–A208.
[6] M. Winter, Zeitschrift Für Physikalische Chemie – International Journal of Research in Physical Chemistry & Chemical Physics 223 (2009) 1395–1406.
[7] H. Buqa, R.I.R. Blyth, P. Golob, B. Evers, I. Schneider, M.V. Santis Alvarez, F. Hofer, F.P. Netzer, M.G. Ramsey, M. Winter, J.O. Besenhard, Ionics 6 (2000) 172–179.
[8] M.E. Spahr, H. Buqa, A. Wursig, D. Goers, L. Hardwick, P. Novak, F. Krumeich, J. Dentzer, C. Vix-Guterl, Journal of Power Sources 153 (2006) 300–311.
[9] D. Aurbach, B. Markovsky, I. Weissman, E. Levi, Y. Ein-Eli, Electrochimica Acta 45 (1999) 67–86.
[10] D. Bar-Tow, E. Peled, L. Burstein, Journal of the Electrochemical Society 146 (1999) 824–832.
[11] M. Winter, P. Novak, A. Monnier, Journal of the Electrochemical Society 145 (1998) 428–436.
[12] R.I.R. Blyth, H. Buqa, F.P. Netzer, M.G. Ramsey, J.O. Besenhard, P. Golob, M. Winter, Applied Surface Science 167 (2000) 99–106.
[13] K. Persson, V.A. Sethuraman, L.J. Hardwick, Y. Hinuma, Y.S. Meng, A. van der Ven, V. Srinivasan, R. Kostecki, G. Ceder, Journal of Physical Chemistry Letters 1 (2010) 1176–1180.
[14] J.P. Olivier, M. Winter, Journal of Power Sources 97–98 (2001) 151–155.
[15] Y.P. Wu, E. Rahm, R. Holze, Journal of Power Sources 114 (2003) 228–236.
[16] H.Y. Wang, M. Yoshio, Journal of Power Sources 93 (2001) 123–129.
[17] I.R.M. Kottegoda, Y. Kadoma, H. Ikuta, Y. Uchimoto, M. Wakihara, Electrochemical and Solid State Letters 5 (2002) A275–A278.
[18] Y. Ein-Eli, V.R. Koch, Journal of the Electrochemical Society 144 (1997) 2968–2973.
[19] Y.P. Wu, C. Jiang, C. Wan, R. Holze, Electrochimica Acta 48 (2003) 867–874.
[20] H. Buqa, P. Golob, M. Winter, J.O. Besenhard, Journal of Power Sources 97–98 (2001) 122–125.
[21] E. Peled, C. Menachem, D. BarTow, A. Melman, Journal of the Electrochemical Society 143 (1996) L4–L7.
[22] D. Goers, H. Buqa, L. Hardwick, A. Wursig, P. Novak, Ionics 9 (2003) 258–265.
[23] S. Ross, J.P. Olivier, Journal of Physical Chemistry 65 (1961) 608-&.
[24] J.P. Olivier, S. Ross, Proceedings of the Royal Society of London Series A – Mathematical and Physical Sciences 265 (1962) 447–454.
[25] P. Tarazona, Physical Review A 31 (1985) 2672–2679.
[26] J. Olivier, The surface heterogeneity of carbon and its assessment, in: E.J. Bottani, J.M.D. Tascón (Eds.), Adsorption by Carbons, 1 ed., Elsevier, New York, 2008, ISBN-10: 0080444644, ISBN-13: 978-0080444642, Chapter 7.
[27] W.W. Huang, P. Frech, Journal of the Electrochemical Society 145 (1998) 765–770.
[28] R. Kostecki, F. McLarnon, Journal of Power Sources 119 (2003) 550–554.
[29] Y.P. Wu, R. Holze, Journal of Solid State Electrochemistry 8 (2003) 73–78.
[30] P. Novak, F. Joho, M. Lanz, B. Rykart, J.C. Panitz, D. Alliata, R. Kotz, O. Haas, Journal of Power Sources 97–98 (2001) 39–46.
[31] F. Joho, B. Rykart, A. Blome, P. Novak, H. Wilhelm, M.E. Spahr, Journal of Power Sources 97–98 (2001) 78–82.